

# A stellar flare-coronal mass ejection event revealed by X-ray plasma motions

C. Argiroffi<sup>1,2\*</sup>, F. Reale<sup>1,2</sup>, J. J. Drake<sup>3</sup>, A. Ciaravella<sup>2</sup>, P. Testa<sup>3</sup>,  
R. Bonito<sup>2</sup>, M. Miceli<sup>1,2</sup>, S. Orlando<sup>2</sup>, and G. Peres<sup>1,2</sup>

<sup>1</sup> University of Palermo, Department of Physics and Chemistry, Piazza del Parlamento 1, 90134, Palermo, Italy.

<sup>2</sup> INAF - Osservatorio Astronomico di Palermo, Piazza del Parlamento 1, 90134, Palermo, Italy.

<sup>3</sup> Smithsonian Astrophysical Observatory, MS-3, 60 Garden Street, Cambridge, MA 02138, USA.

\* costanza.argiroffi@unipa.it

March 12, 2024

Coronal mass ejections (CMEs), often associated with flares<sup>1,2,3</sup>, are the most powerful magnetic phenomena occurring on the Sun. Stars show magnetic activity levels up to  $10^4$  times higher<sup>4</sup>, and CME effects on stellar physics and circumstellar environments are predicted to be significant<sup>5,6,7,8,9</sup>. However, stellar CMEs remain observationally unexplored. Using time-resolved high-resolution X-ray spectroscopy of a stellar flare on the active star HR 9024 observed with Chandra/HETGS, we distinctly detected Doppler shifts in S XVI, Si XIV, and Mg XII lines that indicate upward and downward motions of hot plasmas ( $\sim 10 - 25$  MK) within the flaring loop, with velocity  $v \sim 100 - 400$  km s<sup>-1</sup>, in agreement with a model of flaring magnetic tube. Most notably, we also detected a later blueshift in the O VIII line which reveals an upward motion, with  $v = 90 \pm 30$  km s<sup>-1</sup>, of cool plasma ( $\sim 4$  MK), that we ascribe to a CME coupled to the flare. From this evidence we were able to derive a CME mass of  $1.2^{+2.6}_{-0.8} \times 10^{21}$  g and a CME kinetic energy of  $5.2^{+27.7}_{-3.6} \times 10^{34}$  erg. These values provide clues in the extrapolation of the solar case to higher activity levels, suggesting that CMEs could indeed be a major cause of mass and angular momentum loss.

Intense stellar magnetic fields are responsible for the so-called stellar magnetic activity<sup>10,4</sup>, and for the associated highly energetic phenomena occurring in the outer stellar atmosphere. CMEs, the most energetic coronal phenomena, are observed only on the Sun, because their detection and identification needs spatial resolution.

CMEs are closely linked to flares<sup>3</sup>. In the standard scenario<sup>11</sup> flares are driven by impulsive magnetic reconnections in the corona. The released energy is

transported along the magnetic field lines and heats the underlying chromosphere, that expands upward at hundreds of km s<sup>-1</sup>, filling the overlying magnetic structure (flare rising phase). Then this plasma gradually cools down radiatively and conductively (flare decay). The flare magnetic drivers often cause also large-scale expulsions of previously confined plasma, CMEs, that carry away large amounts of mass and energy. Solar observations demonstrate that CME occurrence, mass, and kinetic energy increase with increasing flare energy<sup>1,2</sup>, corroborating the flare-CME link.

Active stars have stronger magnetic fields, higher flare energies, hotter and denser coronal plasma<sup>12</sup>. Their activity level, measured by the X-ray to bolometric luminosity ratio,  $L_X/L_{\text{bol}}$ , can be up to  $10^4$  times higher than the solar one. Currently, the properties of stellar CMEs can only be presumed extrapolating the solar flare-CME relation up to several orders of magnitude, even though active stellar coronae differ profoundly from the solar one. This extrapolation suggests that stellar CMEs should cause enormous amounts of mass and kinetic energy loss<sup>6,7,8,9</sup> (up to  $\sim 10^{-9} M_\odot \text{ yr}^{-1}$  and  $\sim 0.1 L_{\text{bol}}$ , respectively), and could significantly influence exoplanets<sup>5</sup>.

Thus far, there have been a few claims of stellar CMEs. Blueshifted components of chromospheric lines were sometimes attributed to CMEs<sup>13,14,15</sup>, but they could also be explained by chromospheric brightenings or evaporation events<sup>16,17</sup>. CMEs were invoked to explain increased X-ray absorption observed during flares<sup>18</sup>. However, the simultaneous variations of flare temperature and emission measure<sup>18</sup> ( $EM$ ) insinuate that the increased absorption can be a spurious result coming from the limited diagnostic power of low-resolution X-ray spectroscopy, combined with the oversimplified assumptions of an isothermal flaring plasma and a constant quiescent corona. CMEs were candidates to explain transient UV/X-rays absorptions observed in the eclipsing precataclysmic bi-

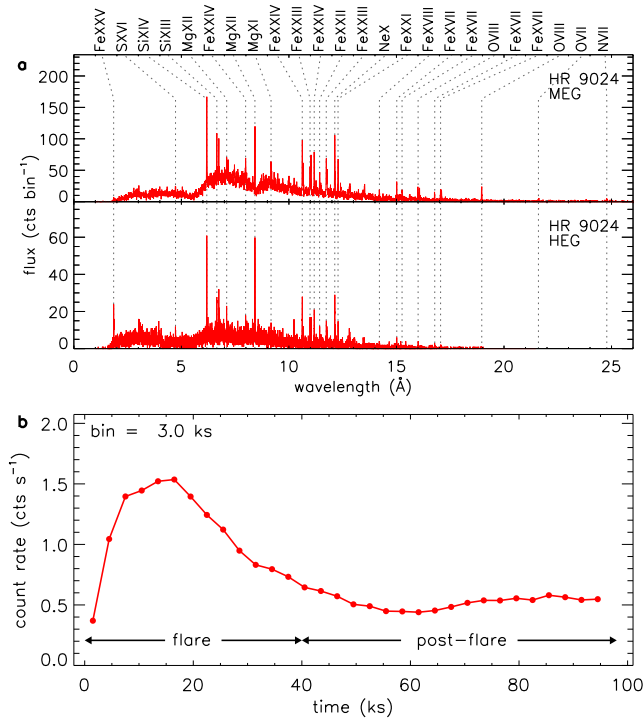


Figure 1: Observed X-ray spectra and light curve of HR 9024. **a**, X-ray spectra collected with the Medium Energy Grating (MEG) and High Energy Grating (HEG) during the 98 ks long *Chandra* observation, with the strongest emission lines labeled. MEG and HEG bin size are 5 and 2.5 mÅ. **b**, X-ray light curve of registered during the *Chandra* observation, obtained from the  $\pm 1$  order spectra of HEG and MEG.

nary V471 Tau<sup>19</sup>. However, such absorptions can equally be produced by a stellar wind<sup>20</sup>. In addition to their ambiguous interpretation, all these candidate detections never provide the CME physical properties, unless substantial assumptions are made.

We present here strong evidence for the detection and identification of a stellar CME, the estimate of the its properties, and the simultaneous monitoring of the associated flare energetics. The Sun indicates that a flare-CME event should produce hot plasma moving upward and downward within the flaring loop, and, after the flare onset, cool plasma in the CME moving upward. Therefore, monitoring the plasma velocity at different temperatures during a stellar flare is a potentially powerful method of searching for CMEs. The unrivalled X-ray spectral resolution of the *Chandra*/HETGS jointly with detailed hydrodynamic (HD) modeling allowed us to investigate a very favorable case: the strong flare<sup>21</sup> observed on the active star HR 9024.

HR 9024 is a G1 III single giant<sup>22</sup>, with  $M_{\star} \sim 2.85 M_{\odot}$  and  $R_{\star} \sim 9.45 R_{\odot}$ , located at 139.5 pc. Its convective envelope and rotational period<sup>23</sup> (24.2 d) indicate that an efficient dynamo is at work<sup>22</sup>, as expected in single G-type giants<sup>24</sup>. Even if some contribution to its magnetic field could have fossil origin<sup>22</sup>,

HR 9024 indeed shows coronal<sup>21</sup> ( $L_X \sim 10^{31} \text{ erg s}^{-1}$ , with  $T \sim 1 - 100 \text{ MK}$ ) and magnetic field properties<sup>22</sup> (a dominant poloidal field with  $B_{\text{max}} \sim 10^2 \text{ G}$ ) analogous to that of other active stars. Therefore, irrespective of the origin of some magnetic components, and bearing in mind that active stars may show diverse magnetic configurations, the coronal phenomena occurring on HR 9024 can be considered as representative of those of active stars.

HR 9024 X-ray spectrum was collected during a 98 ks-long *Chandra*/HETGS observation (Fig. 1a), during which a strong flare (peak luminosity  $\sim 10^{32} \text{ erg s}^{-1}$  and X-ray fluence  $\sim 10^{36} \text{ erg}$ ) was registered (Fig. 1b).

The high energy of this flare maximizes the probability to have an associated CME<sup>1</sup>. The flaring loop located near the stellar disk center, as hinted by the Fe fluorescence<sup>25</sup>, maximizes the possibility to detect radial velocities of both flaring and CME plasmas.

We measured time-resolved individual line positions, considering only strong and isolated lines that probe plasma with  $T$  ranging from 2 to 25 MK (Fig. 2 and Methods and Supplementary Table 1). We found:

- significant blueshifts during the rising phase of the flare in the SXVI line at  $4.73 \text{ \AA}$  ( $-400 \pm 180 \text{ km s}^{-1}$ ) and in the Si XIV line at  $6.18 \text{ \AA}$  ( $-270 \pm 120 \text{ km s}^{-1}$ ), with a 99.99% combined significance of the two line shifts.
- significant redshifts in the Si XIV line at  $6.18 \text{ \AA}$  ( $140 \pm 80 \text{ km s}^{-1}$ ) and Mg XII line at  $8.42 \text{ \AA}$  ( $70 \pm 50$  and  $90 \pm 40 \text{ km s}^{-1}$ ), during the maximum and decay phases of the flare, with a 99.997% combined significance of the three line shifts.
- a significant blueshift in the O VIII line at  $18.97 \text{ \AA}$  ( $-90 \pm 30 \text{ km s}^{-1}$ ), after the flare, significant at 99.9% level.

The first two Doppler shifts tell us that hot flaring plasma moves upward at the beginning of the flare, and then settles back down to the chromosphere, as predicted<sup>11</sup>. We compared the observed velocities with predictions based on the flaring loop model<sup>21</sup> (Methods and Supplementary Fig. 1). For each line and each time interval, we computed the radial velocity corresponding to the predicted line centroid, for different possible inclinations of the flaring loop (identified by the  $\phi$  and  $\theta$  angles defined in Fig. 3a).

The best agreement between observed and predicted velocities (Fig. 3b-f) is obtained assuming a loop observed from above ( $\phi = 0^\circ$  and  $\theta = 90^\circ$ , see Methods), confirming previous independent results<sup>25</sup>. The agreement for the Si XIV and Mg XII lines is striking (Fig. 3c-f). The observed SXVI blueshift, associated with chromospheric plasma upflows, is of the same order but even more extended in time than expected.

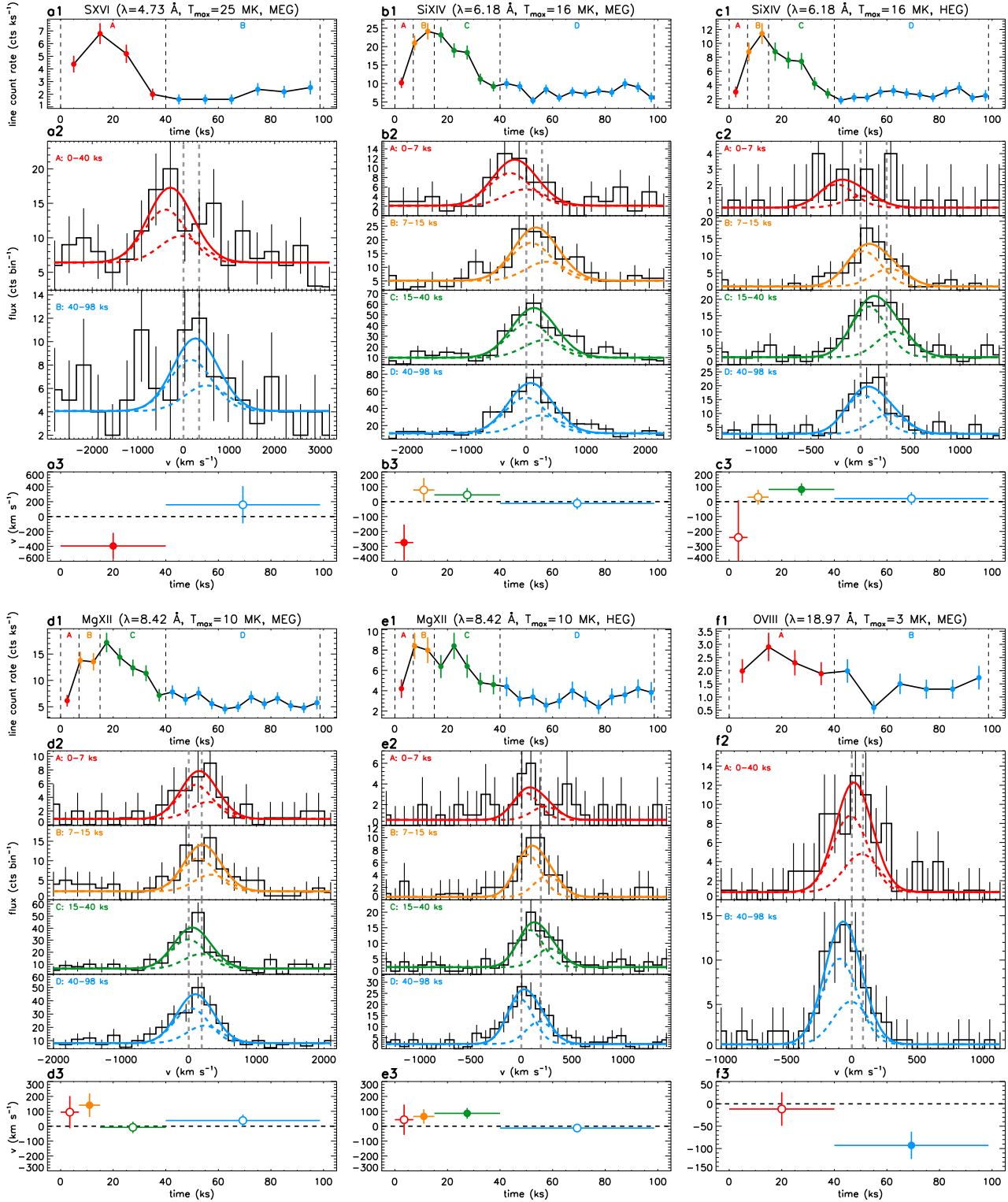


Figure 2: Time-resolved line fits. **a**, Analysis of the SXVI line at 4.73 Å, as registered with the MEG  $\pm 1$  orders. In all plots vertical bars indicate errors at  $1\sigma$ . **a1**, count rate detected in a 0.1 Å interval centered on the line. Letters and colors indicate the different time intervals considered to collect the line profile. **a2**, Observed line profile, in different time intervals (black), with superimposed (in different colors, following the same color-code used for the different time intervals) the corresponding best fit function (with dashed curves corresponding to the two transitions of the Ly $\alpha$  doublet, solid curve to their sum). Vertical dashed gray lines mark the rest position of the two Ly $\alpha$  components. On the  $x$  axis we report the velocity in the stellar reference frame with respect to the bluest Ly $\alpha$  component. **a3**, Line Doppler shifts, in the different time intervals, computed in the stellar reference frame. Horizontal bars specify the time interval. Filled circles mark velocities different from zero at  $1\sigma$  level at least, open circles indicate velocities compatible with zero. The other plots analogously show the time-resolved analysis of: SiXIV line at 6.18 Å as registered with MEG (**b1-b3**) and HEG (**c1-c3**), MgXII line at 8.42 Å as registered with MEG (**d1-d3**) and HEG (**e1-e3**), OVIII line at 18.97 Å as registered with MEG (**f1-f3**).

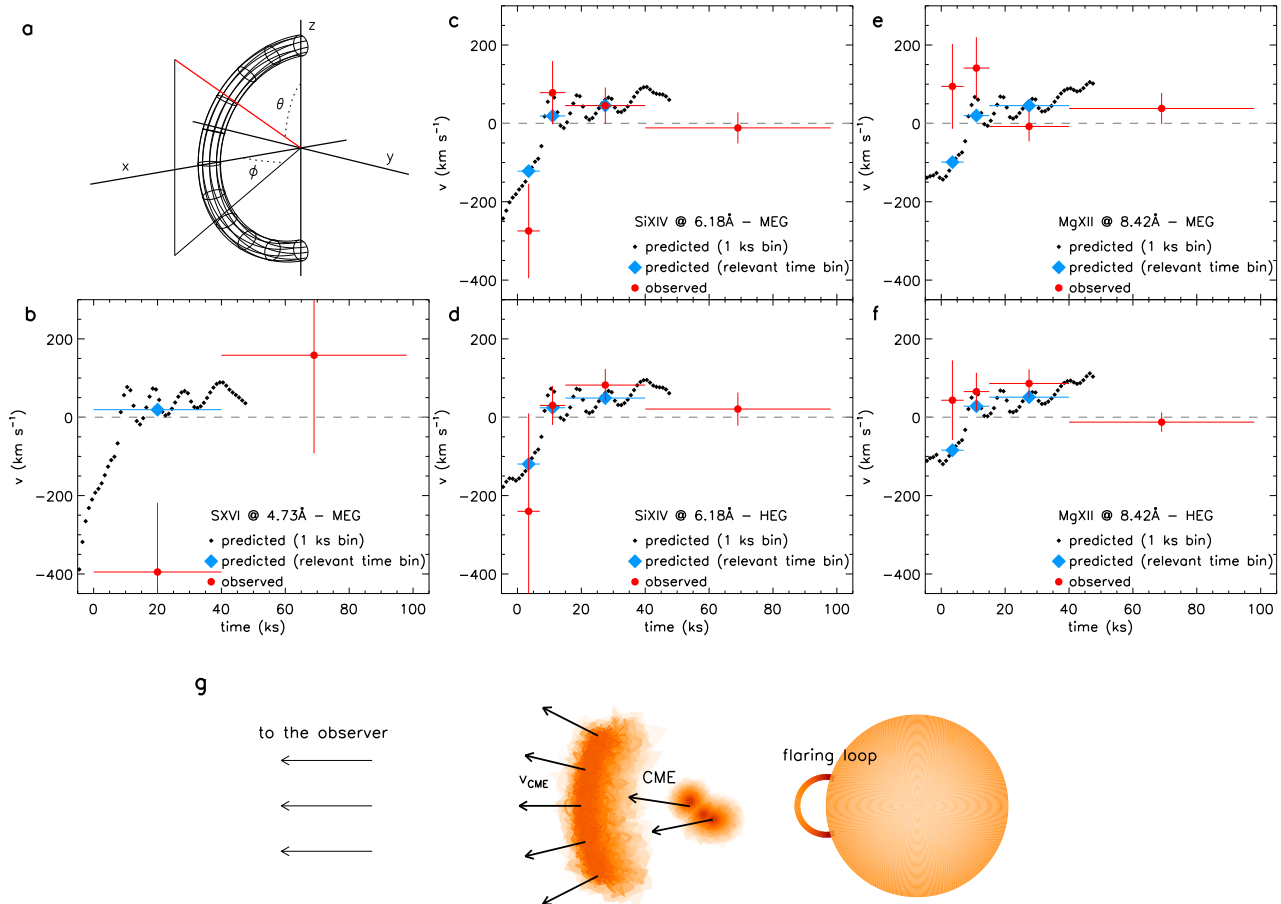


Figure 3: Comparison between observed and predicted velocities. **a**, Viewing geometry of the flaring loop with respect to the observer direction (red line) identified by the  $\phi$  and  $\theta$  angles. **b-f**, Comparison between the line Doppler shifts observed (red circles) and those predicted by the flare model, for  $\phi = 0^\circ$  and  $\theta = 90^\circ$ , for the lines showing significant shifts. Small dark diamonds indicate velocities predicted in 1 ks intervals. Large blue diamonds mark predicted velocities computed integrating the model spectra over the same time intervals considered for the observed spectra. Vertical bars indicate errors at  $1\sigma$ . Horizontal bars mark to the time interval duration. **g**, Schematic illustration of the star/loop/CME configuration.

The agreement obtained for flaring plasma velocities is an important validation of the standard flare model for flare energies up to  $10^{36}$  erg.

Interestingly, we found that the coolest inspected line, O VIII Ly $\alpha$ , that forms at  $\sim 3$  MK, is significantly blueshifted (with  $v = -90 \pm 30$  km s $^{-1}$ ) in the post-flare phase, while no shift is observed during the flare. The low rotational velocity of HR 9024 ( $v \sin i \approx 20$  km s $^{-1}$ )<sup>23</sup> excludes that this motion is due to structures fixed on the stellar surface.

We identify this motion as the signature of a CME (Fig. 3g): it involves only cool plasma, it occurs after a strong flare located near the stellar disk center, and the observed velocity is within the range of solar CME velocities<sup>3</sup> (i.e. 20 – 3000 km s $^{-1}$ ). Solar flares are sometimes followed also by the formation of expanding giant arches<sup>26</sup>. However, this expansion is very slow ( $\sim 1 - 10$  km s $^{-1}$ ) and possibly only apparent, because due to the sequential brightening of different loops<sup>27</sup>, and hence unrelated to Doppler shifts. Although the

extrapolation of the magnetic configuration of the Sun to more active stars is not straightforward, a CME remains the most rational and only explanation.

Hypothesizing that the CME moves exactly along the line of sight, the distance traveled by the CME in the post-flare phase is  $\sim 0.8 R_*$ . Most likely the CME started its motion simultaneously to the flare onset (solar flare and CME onsets differ at most of 1 ks, and the O VIII profile during the flare appears broad, with some blueshifted excess, Fig. 2f). Assuming a constant velocity, the total distance traveled by the CME is  $\sim 1.4 R_*$ . At this distance from the stellar surface the escape velocity is 220 km s $^{-1}$ , larger by a factor of  $\sim 2.4$  than the CME velocity. The real CME velocity, as well as its traveled distance, can be higher because of the possible inclination between the CME trajectory and the line of sight. Assuming an inclination of  $45^\circ$  (i.e. the maximum separation angle for solar flare-CME pairs<sup>1,2</sup>) the ratio between the local escape velocity and the real CME velocity would reduce to  $\sim 1.6$ .

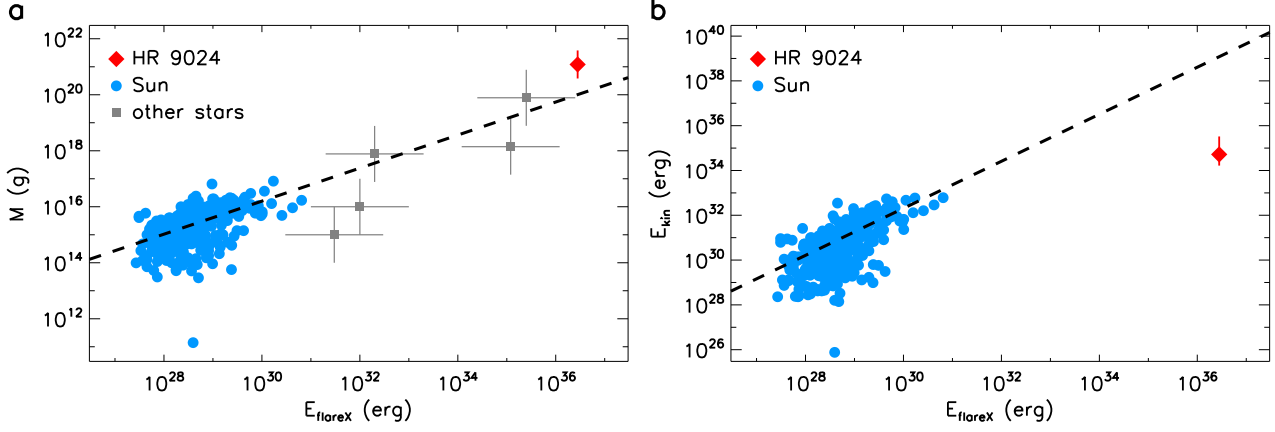


Figure 4: Extrapolation of the solar flare-CME relation. Mass  $M$  (a) and kinetic energy  $E_{\text{kin}}$  (b) of solar CMEs, as a function of the X-ray fluence of the associated flares<sup>1</sup>, with the corresponding power-law relations<sup>7</sup>, compared to the analogous properties of the observed flare-CME pair on HR 9024, and that of other candidate stellar CMEs<sup>9</sup>.

The initial CME mechanical energy has however a minor importance in determining the CME ending. Solar CMEs follow non-ballistic motions. Magnetic forces and wind interactions often cause strong outward acceleration up to heights of several solar radii<sup>3</sup>. The detected CME on HR 9024 shows indeed a velocity approximately constant during the post-flare phase ( $-100 \pm 50$  and  $-80 \pm 50 \text{ km s}^{-1}$  in the 40 – 70 and 70 – 98 ks time intervals, respectively), indicating that strong magnetic forces act on the CME balancing the stellar gravity. Having no data afterwards, we cannot firmly conclude whether the CME does eventually escape to infinity.

Assuming that the post-flare O VIII line entirely comes from the CME, and inferring a CME temperature of  $4 \pm 1 \text{ MK}$ , we derive an  $EM$  of  $(2.8 \pm 1.0) \times 10^{53} \text{ cm}^{-3}$  (see Methods and Supplementary Table 2). As in hot plasmas of solar CMEs, we expect that the CME plasma is optically thin and that, in the observed interval, there is no significant heating source<sup>28</sup>. The duration of the observed CME X-ray emission (stable in the post-flare phase) indicates a radiative cooling time  $\tau > 60 \text{ ks}$ . Being conservative, we assumed  $\tau \sim 200 \text{ ks}$  and a factor of 10 for its confidence interval (i.e.  $60 \text{ ks} < \tau < 600 \text{ ks}$ ). From that we inferred the CME density ( $n_e$ ), volume ( $V$ ), mass ( $M$ ), and kinetic energy ( $E_{\text{kin}}$ , see Methods and Supplementary Table 2, obtaining:

$$\begin{aligned} n_e &= (5.5^{+11.8}_{-3.7}) \times 10^8 \text{ cm}^{-3}, \\ V &= (1.1^{+10.3}_{-1.0}) \times 10^{36} \text{ cm}^3, \\ M &= (1.2^{+2.6}_{-0.8}) \times 10^{21} \text{ g}, \\ E_{\text{kin}} &= (5.2^{+27.7}_{-3.6}) \times 10^{34} \text{ erg}. \end{aligned}$$

Computing also the X-ray flare fluence ( $E_{\text{flareX}} \approx 2.8 \times 10^{36} \text{ erg}$ ), we can compare this flare-CME pair with the solar ones (Fig. 4). The inferred CME mass

suggests that the correlation with the flare energy, observed for the Sun<sup>6,7</sup>, might hold also for stronger flares at higher activity levels. Despite their unsettled identification (as CMEs or chromospheric evaporation), unconstrained mass estimate (the reported values are lower limits<sup>9</sup>), and lack of X-ray coverage (X-ray flare fluence was assumed to be comparable to that in the  $U$  band<sup>9</sup>), the previous candidate stellar CMEs<sup>9</sup> (gray squares in Fig. 4a) also agree with this high-energy extrapolation. Conversely, the obtained CME kinetic energy is  $\sim 10^4$  less than expected from solar data extrapolations (Fig. 4b).

Therefore, CMEs of active stars may not be a scaled version of solar CMEs. In terms of the amount of mass ejected, the CME formation mechanism appears to scale smoothly from the solar case to higher flare energy and higher magnetic activity level. In terms of kinematics, remembering that solar CMEs can experience acceleration both in the low corona ( $< 2 R_{\odot}$ ) or at large distances<sup>3</sup>, the CME acceleration mechanism appears instead less efficient, possibly suggesting a different energy partition in the flare-CME pair.

These CME parameters (i.e. a mass compatible with solar extrapolations, and a significantly reduced  $E_{\text{kin}}$ ) fit well with magnetohydrodynamic models<sup>29,30</sup>, indicating that the balance between the magnetic forces acting on the CME can be different on active stars, with a higher efficiency of the inward force due to the magnetic tension of the overlying large-scale field with respect to the outward force due to the magnetic pressure of the flux rope.

As integrated effect, assuming that the observed CME eventually escapes the star, the inferred large CME mass supports the hypothesis that CMEs can be a major cause of mass and angular momentum loss in active stars<sup>6,7,8,9</sup>, even if it remains unclear down to what energy flares can cause eruptions in active stars. The diminished  $E_{\text{kin}}$  to  $E_{\text{flareX}}$  ratio indicates instead

that, at high activity levels, the energy fraction carried out by CMEs diminishes. That supports that magnetic activity at most extracts  $\sim 10^{-3}$  of the stellar bolometric luminosity, and excludes the huge magnetic energy budget implied by solar case extrapolations to higher activity levels<sup>7</sup>.

## Methods

### Data analysis

HR 9024 was observed on August 2001 for 98 ks with Chandra/HETGS (ObsID 1892). This instrument configuration consists of two transmission gratings, the HEG and the MEG, used with the ACIS-S detector. The two gratings simultaneously collect spectra in the 1.2 – 15 Å (HEG) and 2.5 – 31 Å (MEG) intervals, with a spectral resolution (FWHM) of 12 and 23 mÅ, respectively. In this work we inspected the HEG and MEG spectra of HR 9024 separately, each one obtained by adding +1 and –1 diffraction orders. The data have been retrieved from the Grating-Data Archive and Catalog<sup>31</sup>.

The wavelength calibration of the Chandra/HETGS, allows velocity measurements down to a few tens of  $\text{km s}^{-1}$  by comparing line positions within and between observations, as confirmed by several studies<sup>32,33,34,35</sup>. Hence the Chandra/HETGS is well suited to measure the velocity of flaring and CME plasmas.

To search for Doppler shifts we selected a sample of strong and isolated emission lines (Supplementary Table 1). Inspecting isolated lines allows us to avoid line position uncertainties due to line blending. Moreover monitoring individual lines, instead of inspecting the whole spectrum, allows us to probe separately plasma components at different temperatures. The selected line sample is composed of: Lyman series lines of N VII, O VIII, Mg XII, Si XIV, and S XVI; He-like ion lines of Mg XI, Si XIII, and O VII; and the strong Fe XVII lines in the 15 – 17 Å range. We did not inspect the Ne IX and Ne X lines, because of the severe blendings with Fe lines. The maximum formation temperature of the inspected line sample ranges from 2 to 25 MK.

We determined the position of each selected line by least-squares fitting its observed profile in different time intervals. The selected duration of the inspected time intervals is aimed at: a) separating the phases corresponding to significantly different predicted velocities (HD model, described below and in Supplementary Fig. 1, predicts high upward velocity during the rising phase, and slower downward motions during the maximum and decay phases, Fig. 3b-f); b) collecting enough counts to perform the line fit. For each line we performed the fit in a small wavelength interval, with width  $\sim 0.1 - 0.2$  Å, around the line rest wavelength. As best-fit function we assumed a Gaussian plus a constant, to take also the continuum emission

into account. The  $\sigma$  of the Gaussian was fixed to the predicted value<sup>32</sup>. Since the Ly $\alpha$  lines are doublets, we fit their observed profiles with two Gaussians, with relative positions fixed to the predicted wavelength difference, and relative intensity fixed to the predicted value (i.e. 2 : 1 in the optically thin emission regime).

The observed line shifts, with respect to the predicted wavelengths, provide velocity with respect to the Chandra satellite reference frame ( $v_{\text{sat}}$ ). We assumed that these velocities are the same as that with respect to the Earth, because of the low satellite velocity (at most of  $\sim 1 - 2 \text{ km s}^{-1}$  with respect to the Earth). We computed the plasma velocity in the stellar reference frame as  $v = v_{\text{sat}} + v_{\text{E}} - v_{\star}$ , where  $v_{\text{E}}$  is the line-of-sight Earth velocity at the epoch of the observation (i.e.  $v_{\text{E}} = 19.9 \text{ km s}^{-1}$  in the heliocentric reference frame), and  $v_{\star}$  is the radial velocity of HR 9024 (i.e.  $v_{\star} = -1.6 \text{ km s}^{-1}$  in the heliocentric reference frame). Throughout the paper we indicated outward motions with respect to us (redshifts) with positive radial velocities, and inward motions with respect to us (blueshifts) with negative radial velocities.

The lines showed in Fig. 2, and discussed in the paper are the ones for which a significant shift was detected in at least one time interval. For lines with  $S/N$  ratio high enough, we analyzed both HEG and MEG spectra. Because of the different  $S/N$  and spectral resolution between corresponding MEG and HEG spectra (with MEG providing higher  $S/N$  but lower spectral resolution than HEG), significant line shifts were sometimes found only in one grating. In these cases, the shift measurements obtained with the two gratings (even if only one was significantly different from zero) were anyhow compatible among themselves.

We display in Supplementary Fig. 2 the observed and predicted shifts for those lines with a  $S/N$  high enough to allow time-resolved spectral fitting, for which no significant shift was obtained. For the hottest of these lines (i.e. the Si XIII at 6.65 Å, and the Mg XII at 7.11 Å), the expected radial velocities during the flare evolution are high enough to be detectable with the Chandra gratings. However, the low  $S/N$  collected for these lines (total line counts are listed in Supplementary Table 1) avoids precise shift measurements and/or prevents from us exploring time bins short enough. For the coolest of these latter lines (i.e. all the Fe XVII lines), in addition to the low  $S/N$ , significantly smaller shifts only in very short time intervals are expected. Notice that the large redshifted velocities of  $\sim 200 \text{ km s}^{-1}$  expected for the very final part of the flare correspond to phases in which the line fluxes become negligible, because of the vanishing  $EM$  of the flaring loop.

## Flaring loop model and line emission synthesis

To infer the expected line Doppler shifts due to plasma motions during the flare, and to constrain the loop orientation with respect to the observer, we considered the flare loop model presented by Testa et al.<sup>21</sup>. This model assumes that: the stellar magnetic field is so strong as to confine the plasma inside single closed magnetic tubes (coronal loops); the footpoints of the flaring loop are anchored to the photosphere; the flaring plasma moves and transports energy only along the field lines, and its evolution can be described with a 1D HD model along the tube. The HD equations for a compressible plasma fluid are solved numerically to obtain the evolution of the plasma density, temperature, and velocity along the loop. The flare is triggered with a strong heat pulse injected inside an initially hydrostatic and relatively cool loop atmosphere which includes a tenuous corona linked to a dense chromosphere. Tuning the model parameters to reproduce the observed evolution of  $T$  and  $EM$  during the flare, it came out that: the total loop length is  $5 \times 10^{11}$  cm; the duration and rate of the heat pulse are 15 ks and  $1.2 \times 10^{33}$  erg s<sup>-1</sup>, respectively, for a total injected energy of  $\sim 1.7 \times 10^{37}$  erg; the pulse heats the plasma to a maximum temperature of  $\sim 150$  MK and makes it expand from the chromosphere at a maximum speed of  $\sim 1800$  km s<sup>-1</sup>, which drops rapidly below 400 km s<sup>-1</sup> after a few ks since the heat pulse has started. The evolution of velocity, temperature, and  $EM$  of the flaring loop are shown in Supplementary Fig. 1.

The X-ray emission of the flaring loop is assumed to be optically thin. Line emissivities were retrieved from the APED database<sup>36</sup>. We computed line emission from the flaring loop considering both short time intervals (i.e. 1 ks), to monitor line profiles on time scales corresponding to the characteristic time scales of the flaring loop variability, and long time intervals (i.e. corresponding to that adopted for the observed line profiles) to perform a proper comparison between observed and predicted line shifts.

We computed predicted line profiles for different viewing geometries of the loop, exploring the range  $0^\circ < \phi < 90^\circ$  and  $0^\circ < \theta < 90^\circ$  (Fig. 3a). The  $\phi$  angle determines a global scaling factor in the predicted line shifts, with  $\phi \sim 0^\circ$  corresponding to the largest shifts, and  $\phi \sim 90^\circ$  corresponding to no shift. Taking the possible values of  $\theta$  into account, and considering that the footpoint portions of the loop are responsible for the highest emission and highest velocity, (Supplementary Fig. 1), configurations with  $\theta \sim 90^\circ$  maximize the line shifts, while configurations with  $\theta \sim 0^\circ$  minimize the line shifts (causing also some line broadening, because of the simultaneous redshifted and blueshifted contributions originating in the motions of plasma located near the loop apex). We found that only for  $\phi = 0^\circ$  and  $\theta = 90^\circ$  the predicted shifts are large enough to

reproduce that observed.

In general, since the coronal part of the loop is most of the flaring volume, filled with upflowing plasma at temperatures  $\geq 50 - 100$  MK, we would expect Doppler shifts in highly ionized lines, like Ca XX formed at  $\sim 50$  MK, but they are not detected<sup>21</sup>. Instead, we detected Doppler shifts, associated with motions of flaring plasma, in lines at  $T \sim 10 - 25$  MK, hence emitted mostly at the loop footpoints. This happens because Doppler shift measurements are best obtained in lines detected with high  $S/N$  ratio. The spatial distributions of  $T$  and  $EM$  along the flaring loop determine that hotter lines, mainly emitted by higher loop portions where the  $EM$  is lower, have lower  $S/N$  with respect to cooler lines, that come primarily from lower loop portions where the  $EM$  is higher.

Finally, the agreement obtained between observed and predicted velocities, considering that this HD flare model was tuned to match only X-ray flux and plasma temperature, support the hypothesis of a flare occurring in a single loop, and allows us to confirming the loop geometry, the temporal and spatial distribution of heating, and the kinetic energy budget involved in plasma motions.

## Cool plasma velocity after the flare

The blueshifted emission, detected at  $3\sigma$  level in the post-flare phases in the O VIII line, is per se robust because of the accuracy of the Chandra wavelength calibration: in a sample of active stars<sup>32</sup> the shift displayed by this line is always smaller than 13 km s<sup>-1</sup>. To further corroborate this detection we anyhow inspected the N VII Ly $\alpha$  at 24.78 Å that forms mainly at 2 MK. This line does not have enough counts to fit its profile. Selecting the post-flare interval, the average position of the photons detected in the  $\pm 1000$  km s<sup>-1</sup> interval around its rest position is  $-110 \pm 80$  km s<sup>-1</sup>, thus confirming the cool plasma blueshift at  $1.4\sigma$  level. These two simultaneous blueshifts further increase the significance of the detected plasma motion. Summarizing, considering all the inspected lines in the post-flare phase, plasma at  $T \lesssim 4$  MK moves upward, hence it is located in the CME, possibly representing its hottest component; conversely, plasma with  $T \gtrsim 5$  MK appears motionless, and hence situated in stable coronal structures.

## CME parameter estimation

Assuming that the O VIII emission is entirely due to a CME, we have a direct measurement of the CME average radial velocity,  $v$ , and of the CME total luminosity in the O VIII line,  $L_{\text{O VIII}}$ , corrected for the interstellar absorption<sup>37</sup> of  $4 \times 10^{20}$  cm<sup>-2</sup>. To infer the temperature  $T$  of the CME we considered the observed post-flare line ratio between the O VII resonance line at 21.60 Å

and the O VIII Ly $\alpha$ . This ratio provides a lower limit<sup>36</sup> of 3 MK for  $T$ . In addition, the Fe XVII lines, that form mainly at 5 MK, do not show any blueshift, indicating that they are produced by coronal loops and not by the CME. We therefore deduced that the CME temperature  $T$  should be  $4 \pm 1$  MK. We do not detect any significant decline in the O VIII line flux. This suggests that the CME likely moves as a coherent structure, without experiencing significant adiabatic expansion, in spite of the large distance travelled in the related time range.

The line luminosity together with the plasma temperature allow us to determine the CME emission measure  $EM$  as:

$$EM = \frac{L_{\text{O VIII}}}{A_{\text{O}} G(T)}$$

where  $G(T)$  is the line emissivity function (APED database<sup>36</sup>), and  $A_{\text{O}}$  is the oxygen abundance (we adopted the abundances inferred from the post-flare emission<sup>21</sup>).

The CME emission is observed for  $\sim 60$  ks. Therefore, its radiative cooling time  $\tau$  must be longer. We assumed  $\tau = 200$  ks, with a confidence interval of a factor 10, that corresponds to  $60 \text{ ks} < \tau < 600 \text{ ks}$ . By also assuming that, during the observed emission, there is no heating source in the CME, that its emission is optically thin, and that the hydrogen to electron density ratio  $n_{\text{H}}/n_{\text{e}}$  is 0.83 (value corresponding to high-temperature plasma with cosmic abundances), we can estimate the CME electron density from:

$$E_{\text{int}} = \frac{3}{2} (n_{\text{e}} + n_{\text{H}}) V k_{\text{B}} T$$

$$\dot{E}_{\text{rad}} = n_{\text{e}} n_{\text{H}} V \Lambda(T)$$

$$\tau = \frac{E_{\text{int}}}{\dot{E}_{\text{rad}}} \Rightarrow n_{\text{e}} = \frac{3}{2} \left( \frac{n_{\text{e}}}{n_{\text{H}}} + 1 \right) \frac{k_{\text{B}} T}{\tau \Lambda(T)}$$

where  $E_{\text{int}}$  is the CME internal energy,  $\dot{E}_{\text{rad}}$  is the radiative loss rate,  $V$  is the CME volume, and  $\Lambda(T)$  is the radiative loss function per  $EM$  unit in the  $1 - 2000 \text{ \AA}$  wavelength interval, computed assuming the plasma emissivities of the APED database<sup>36</sup>. The estimates for  $EM$  and  $n_{\text{e}}$  finally allow us to derive the volume  $V$ , mass  $M$ , and kinetic energy  $E_{\text{kin}}$  of the CME:

$$V = \frac{EM}{n_{\text{e}} n_{\text{H}}}$$

$$M = V n_{\text{H}} m = \frac{EM}{n_{\text{e}}} m$$

$$E_{\text{kin}} = \frac{1}{2} M v^2$$

where  $m$  is the mean mass per hydrogen atom. All the values of the relevant CME parameters are reported in Supplementary Table 2.

In the estimation of the uncertainty of  $n_{\text{e}}$ ,  $V$ ,  $M$ , and  $E_{\text{kin}}$ , we considered only the uncertainty on  $\tau$ , because it is significantly larger than the uncertainties on  $T$  and  $EM$ . Only in the computation of the upper limit of the confidence interval of  $E_{\text{kin}}$  we included also a factor related to the possible flare-CME separation angle, in agreement with solar observations<sup>1,2</sup> that indicate at most separations of  $45^\circ$ . The observed O VIII line does not show significant broadening in the post-flare interval, its width is in fact compatible with the instrumental width. Therefore, velocity dispersion along the line of sight in the CME plasma is expected to be small ( $\leq 100 \text{ km s}^{-1}$ ), corroborating further the inferred  $E_{\text{kin}}$  value.

We finally notice that both  $M$  and  $E_{\text{kin}}$  are directly proportional to  $\tau$ . Therefore, the strict lower limit of 60 ks, provided by the stable post-flare emission in the O VIII, corresponds to the lower limits of the confidence intervals of  $M$  and  $E_{\text{kin}}$ . Conversely, the already large upper limit on  $M$  is an a posteriori confirmation on the adopted upper limit on  $\tau$ . Moreover, the reasonable assumptions made for the  $\tau$  confidence interval is also supported by the  $n_{\text{e}}$  value inferred, neatly compatible with the density observed in solar CMEs<sup>28,38,39</sup>.

## Data Availability

The Chandra dataset analyzed in this work (ObsID 1892) can be accessed from <http://cxc.harvard.edu/>. The data that support plots and findings of this study are available from the corresponding author upon reasonable request.

## References

- [1] Yashiro, S. & Gopalswamy, N. Statistical relationship between solar flares and coronal mass ejections. In Gopalswamy, N. & Webb, D. F. (eds.) *Universal Heliophysical Processes*, vol. 257 of *IAU Symp.*, 233–243 (2009).
- [2] Aarnio, A. N., Stassun, K. G., Hughes, W. J. & McGregor, S. L. Solar Flares and Coronal Mass Ejections: A Statistically Determined Flare Flux - CME Mass Correlation. *Sol. Phys.* **268**, 195–212 (2011).
- [3] Webb, D. F. & Howard, T. A. Coronal Mass Ejections: Observations. *Living Rev. Sol. Phys.* **9**, 3 (2012).
- [4] Wright, N. J., Drake, J. J., Mamajek, E. E. & Henry, G. W. The Stellar-activity-Rotation Relationship and the Evolution of Stellar Dynamos. *Astrophys. J.* **743**, 48 (2011).
- [5] Khodachenko, M. L. *et al.* Coronal Mass Ejection (CME) Activity of Low Mass M Stars as An Important Factor for The Habitability of Terrestrial

- Exoplanets. I. CME Impact on Expected Magnetospheres of Earth-Like Exoplanets in Close-In Habitable Zones. *Astrobiology* **7**, 167–184 (2007).
- [6] Aarnio, A. N., Matt, S. P. & Stassun, K. G. Mass Loss in Pre-main-sequence Stars via Coronal Mass Ejections and Implications for Angular Momentum Loss. *Astrophys. J.* **760**, 9 (2012).
- [7] Drake, J. J., Cohen, O., Yashiro, S. & Gopalswamy, N. Implications of Mass and Energy Loss due to Coronal Mass Ejections on Magnetically Active Stars. *Astrophys. J.* **764**, 170 (2013).
- [8] Osten, R. A. & Wolk, S. J. Connecting Flares and Transient Mass-loss Events in Magnetically Active Stars. *Astrophys. J.* **809**, 79 (2015).
- [9] Odert, P., Leitzinger, M., Hanslmeier, A. & Lammer, H. Stellar coronal mass ejections - I. Estimating occurrence frequencies and mass-loss rates. *Mon. Not. R. Astron. Soc.* **472**, 876–890 (2017).
- [10] Noyes, R. W., Hartmann, L. W., Baliunas, S. L., Duncan, D. K. & Vaughan, A. H. Rotation, convection, and magnetic activity in lower main-sequence stars. *Astrophys. J.* **279**, 763–777 (1984).
- [11] Shibata, K. & Magara, T. Solar Flares: Magnetohydrodynamic Processes. *Living Rev. Sol. Phys.* **8**, 6 (2011).
- [12] Güdel, M. X-ray astronomy of stellar coronae. *Annu. Rev. Astron. Astrophys.* **12**, 71–237 (2004).
- [13] Houdebine, E. R., Foing, B. H. & Rodono, M. Dynamics of flares on late-type dMe stars. I - Flare mass ejections and stellar evolution. *Astron. Astrophys.* **238**, 249–255 (1990).
- [14] Vida, K. *et al.* Investigating magnetic activity in very stable stellar magnetic fields. Long-term photometric and spectroscopic study of the fully convective M4 dwarf V374 Pegasi. *Astron. Astrophys.* **590**, A11 (2016).
- [15] Vida, K. *et al.* The quest for stellar coronal mass ejections in late-type stars. I. Investigating Balmer-line asymmetries of single stars in Virtual Observatory data. *Astron. Astrophys.* **623**, A49 (2019).
- [16] Gunn, A. G., Doyle, J. G., Mathioudakis, M., Houdebine, E. R. & Avgoloupis, S. High-velocity evaporation during a flare on AT Microscopii. *Astron. Astrophys.* **285**, 489–496 (1994).
- [17] Berdyugina, S. V., Ilyin, I. & Tuominen, I. The active RS Canum Venaticorum binary II Pegasi. III. Chromospheric emission and flares in 1994–1996. *Astron. Astrophys.* **349**, 863–872 (1999).
- [18] Moschou, S.-P., Drake, J. J., Cohen, O., Alvarado-Gomez, J. D. & Garraffo, C. A Monster CME Obscuring a Demon Star Flare. *Astrophys. J.* **850**, 191 (2017).
- [19] Wheatley, P. J. ROSAT observations of V471 Tauri, showing that stellar activity is determined by rotation, not age. *Mon. Not. R. Astron. Soc.* **297**, 1145–1150 (1998).
- [20] Mullan, D. J., Sion, E. M., Bruhweiler, F. C. & Carpenter, K. G. Evidence for a cool wind from the K2 dwarf in the detached binary V471 Tauri. *Astrophys. J. Lett.* **339**, L33–L36 (1989).
- [21] Testa, P., Reale, F., Garcia-Alvarez, D. & Huenemoerder, D. P. Detailed Diagnostics of an X-Ray Flare in the Single Giant HR 9024. *Astrophys. J.* **663**, 1232–1243 (2007).
- [22] Borisova, A. *et al.* The different origins of magnetic fields and activity in the Hertzsprung gap stars, OU Andromedae and 31 Comae. *Astron. Astrophys.* **591**, A57 (2016).
- [23] Strassmeier, K. G., Serkowitsch, E. & Granzer, T. Starspot photometry with robotic telescopes. UBVR(I)C and by light curves of 47 active stars in 1996/97. *Astron. Astrophys. Suppl. Ser.* **140**, 29–53 (1999).
- [24] Pizzolato, N., Maggio, A. & Sciortino, S. Evolution of X-ray activity of 1–3  $M_{\text{sun}}$  late-type stars in early post-main-sequence phases. *Astron. Astrophys.* **361**, 614–628 (2000).
- [25] Testa, P. *et al.* Geometry Diagnostics of a Stellar Flare from Fluorescent X-Rays. *Astrophys. J.* **675**, L97 (2008).
- [26] Švestka, Z. Speeds of Rising Post-Flare Structures. *Sol. Phys.* **169**, 403–413 (1996).
- [27] West, M. J. & Seaton, D. B. SWAP Observations of Post-flare Giant Arches in the Long-Duration 14 October 2014 Solar Eruption. *Astrophys. J. Lett.* **801**, L6 (2015).
- [28] Landi, E., Raymond, J. C., Miralles, M. P. & Hara, H. Physical Conditions in a Coronal Mass Ejection from Hinode, Stereo, and SOHO Observations. *Astrophys. J.* **711**, 75–98 (2010).
- [29] Drake, J. J., Cohen, O., Garraffo, C. & Kashyap, V. Stellar flares and the dark energy of CMEs. In Kosovichev, A. G., Hawley, S. L. & Heinzel, P. (eds.) *Solar and Stellar Flares and their Effects on Planets*, vol. 320 of *IAU Symp.*, 196–201 (2016).

- [30] Alvarado-Gómez, J. D., Drake, J. J., Cohen, O., Moschou, S. P. & Garraffo, C. Suppression of Coronal Mass Ejections in Active Stars by an Overlying Large-scale Magnetic Field: A Numerical Study. *Astrophys. J.* **862**, 93 (2018).
- [31] Huenemoerder, D. P. *et al.* TGCat: The Chandra Transmission Grating Data Catalog and Archive. *Astron. J.* **141**, 129 (2011).
- [32] Argiroffi, C. *et al.* Redshifted X-rays from the material accreting onto TW Hydrae: Evidence of a low-latitude accretion spot. *Astron. Astrophys.* **607**, A14 (2017).
- [33] Brickhouse, N. S., Dupree, A. K. & Young, P. R. X-Ray Doppler Imaging of 44i Bootis with Chandra. *Astrophys. J.* **562**, L75–L78 (2001).
- [34] Chung, S. M., Drake, J. J., Kashyap, V. L., Lin, L. W. & Ratzlaff, P. W. Doppler Shifts and Broadening and the Structure of the X-Ray Emission from Algol. *Astrophys. J.* **606**, 1184–1195 (2004).
- [35] Ishibashi, K., Dewey, D., Huenemoerder, D. P. & Testa, P. Chandra/HETGS Observations of the Capella System: The Primary as a Dominating X-Ray Source. *Astrophys. J.* **644**, L117–L120 (2006).
- [36] Smith, R. K., Brickhouse, N. S., Liedahl, D. A. & Raymond, J. C. Collisional Plasma Models with APEC/APED: Emission-Line Diagnostics of Hydrogen-like and Helium-like Ions. *Astrophys. J.* **556**, L91–L95 (2001).
- [37] Singh, K. P., Drake, S. A., White, N. E. & Simon, T. ROSAT Observations of Five Chromospherically Active Stars. *Astron. J.* **112**, 221 (1996).
- [38] Cheng, X., Zhang, J., Saar, S. H. & Ding, M. D. Differential Emission Measure Analysis of Multiple Structural Components of Coronal Mass Ejections in the Inner Corona. *Astrophys. J.* **761**, 62 (2012).
- [39] Landi, E., Miralles, M. P., Raymond, J. C. & Hara, H. Hot Plasma Associated with a Coronal Mass Ejection. *Astrophys. J.* **778**, 29 (2013).

C.A. and J.J.D. contributed to analysis of observational data. F.R. contributed to the HD model development, and C.A. to the synthesis of the model line profile.

### Competing interests

The authors declare no competing financial interests.

### Additional information

Correspondence and requests for materials should be addressed to C. Argiroffi.

### Acknowledgements

The authors acknowledges modest financial contribution from the agreement ASI-INAF n.2017-14.H.O.

### Author contributions

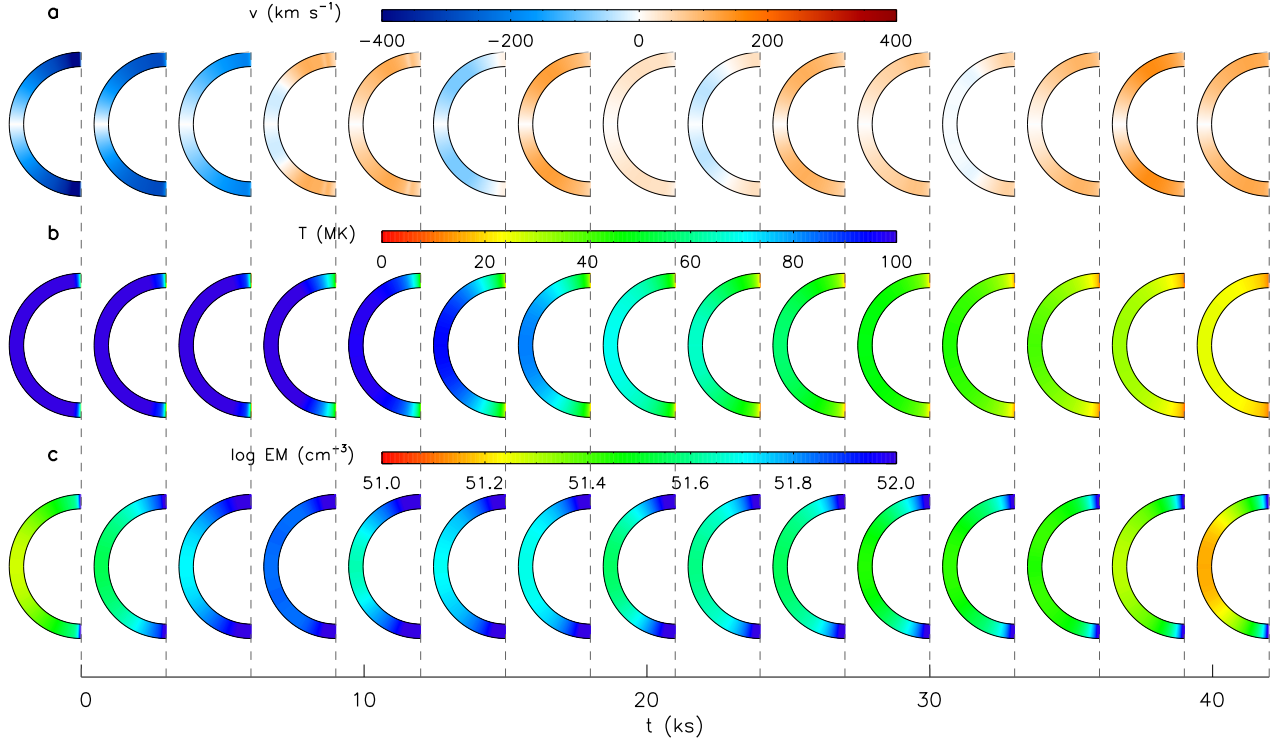
C.A., F.R., J.J.D., A.C., P.T., R.B., M.M., S.O., G.P. contributed to scientific discussion and text writing.

## Supplementary Information

Supplementary Table 1: Selected emission lines

| Index <sup>a</sup> | $\lambda^b$<br>(Å) | Elem.  | $T_{\max}^c$<br>(MK) | $F_{\text{MEG}}^d$<br>(cts) | $F_{\text{HEG}}^e$<br>(cts) |
|--------------------|--------------------|--------|----------------------|-----------------------------|-----------------------------|
| 1a                 | 4.7274             | SXVI   | 25.1                 | $66 \pm 15^f$               | $21 \pm 10$                 |
| 1b                 | 4.7328             | SXVI   | 25.1                 | ...                         | ...                         |
| 2a                 | 6.1804             | SiXIV  | 15.8                 | $505 \pm 31^f$              | $231 \pm 21^f$              |
| 2b                 | 6.1858             | SiXIV  | 15.8                 | ...                         | ...                         |
| 3                  | 6.6479             | SiXIII | 10.0                 | $218 \pm 24$                | $83 \pm 14$                 |
| 4                  | 6.7403             | SiXIII | 10.0                 | $185 \pm 23$                | $83 \pm 14$                 |
| 5a                 | 7.1058             | MgXII  | 10.0                 | $115 \pm 23$                | $34 \pm 11$                 |
| 5b                 | 7.1069             | MgXII  | 10.0                 | ...                         | ...                         |
| 6a                 | 8.4192             | MgXII  | 10.0                 | $345 \pm 26^f$              | $228 \pm 20^f$              |
| 6b                 | 8.4246             | MgXII  | 10.0                 | ...                         | ...                         |
| 7                  | 9.1687             | MgXI   | 6.3                  | $136 \pm 21$                | $35 \pm 11$                 |
| 8                  | 15.0140            | FeXVII | 5.0                  | $62 \pm 14$                 | $12 \pm 7$                  |
| 9a                 | 16.0055            | OVIII  | 3.2                  | $52 \pm 13$                 | $4 \pm 6$                   |
| 9b                 | 16.0067            | OVIII  | 3.2                  | ...                         | ...                         |
| 10                 | 16.7800            | FeXVII | 5.0                  | $53 \pm 12$                 | $7 \pm 6$                   |
| 11                 | 17.0510            | FeXVII | 5.0                  | $55 \pm 12$                 | $5 \pm 6$                   |
| 12                 | 17.0960            | FeXVII | 5.0                  | $56 \pm 12$                 | $4 \pm 6$                   |
| 13a                | 18.9671            | OVIII  | 3.2                  | $112 \pm 14^f$              | $4 \pm 6$                   |
| 13b                | 18.9725            | OVIII  | 3.2                  | ...                         | ...                         |
| 14                 | 21.6015            | OVII   | 2.0                  | $8 \pm 8$                   | ...                         |
| 15a                | 24.7792            | NVII   | 2.0                  | $21 \pm 9$                  | ...                         |
| 15b                | 24.7846            | NVII   | 2.0                  | ...                         | ...                         |

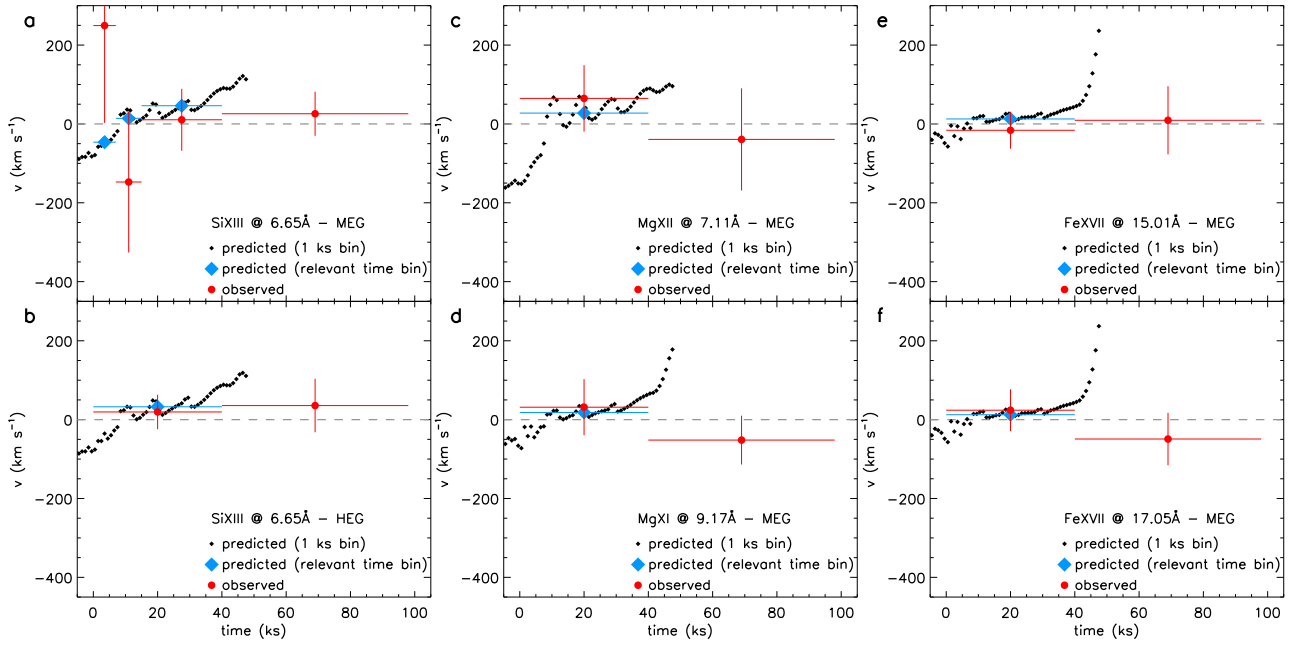
<sup>a</sup> Lines indicated with the same index number, but different letters, are the two components of H-like resonance doublets. <sup>b</sup> Predicted wavelength from the APED database. <sup>c</sup> Temperature of maximum formation of the line. <sup>d</sup> Line counts observed in the MEG spectrum during the whole observation. <sup>e</sup> Line counts observed in the HEG spectrum during the whole observation. <sup>f</sup> Lines for which a significant shift was detected in at least one time interval.



Supplementary Figure 1: Flaring loop model. Time evolution of velocity along the loop (a), temperature (b), and emission measure (c) in the flaring loop, as predicted by the HD model. Negative velocities (marked in blue) correspond to upward motion in the loop, positive velocities (marked in red) correspond to downward motions.

Supplementary Table 2: CME properties

| parameter        | units                  | value                                 |
|------------------|------------------------|---------------------------------------|
| $v$              | ( $\text{km s}^{-1}$ ) | $-90 \pm 30$                          |
| $T$              | (MK)                   | $4.0 \pm 1.0$                         |
| $M$              | ( $g$ )                | $(1.2^{+2.6}_{-0.8}) \times 10^{21}$  |
| $E_{\text{kin}}$ | (erg)                  | $(5.2^{+27.7}_{-3.6}) \times 10^{34}$ |
| $n_e$            | ( $\text{cm}^{-3}$ )   | $(5.5^{+11.8}_{-3.7}) \times 10^8$    |
| $\tau$           | (ks)                   | $200.0^{+400}_{-140}$                 |
| $EM$             | ( $\text{cm}^{-3}$ )   | $(2.8 \pm 1.0) \times 10^{53}$        |
| $V$              | ( $\text{cm}^3$ )      | $(1.1^{+10.3}_{-1.0}) \times 10^{36}$ |



Supplementary Figure 2: Comparison between observed and predicted Doppler shifts for lines showing no significant shifts. Symbols are the same as in Fig. 3.